Available online at www.sciencedirect.com
SCIENCE DIRECT®
ELSEVIER
International Journal of Impact Engineering 32 (2006) 1621–1634
INTERNATIONAL JOURNAL OF IMPACT ENGINEERING
www.elsevier.com/locate/ijimpeng

Some considerations for 3D EFP computations

Gordon R. Johnson*, Robert A. Stryk

Network Computing Services Incorporated, P.O. Box 581459, Minneapolis, MN 55415, USA

Received 17 August 2004; received in revised form 12 January 2005; accepted 14 January 2005
Available online 11 April 2005

Abstract

This article identifies some issues, options and results associated with 3D Explosively Formed Penetrator (EFP) computations. The three broad categories of interest (for Lagrangian computations) are the sliding/contact interfaces, the type and arrangement of elements, and the generation of the grid. The sliding/contact algorithm uses a virtual particle approach that is very robust, and it is described in detail. Tetrahedral elements are considered for both symmetric and non-symmetric arrangement, each with some advantages and disadvantages. A mixed element algorithm is also considered for the non-symmetric arrangement, in an effort to eliminate some of the locking that occurs for the non-symmetric arrangement. Hexahedral (brick) elements are not considered herein, but some of the effects (for tetrahedral elements) also apply to hexahedral elements. For axisymmetric EFPs there are also some trade-offs (symmetric grid vs. equally sized elements) associated with the generation of the grid. Computational results are provided to illustrate each of the issues and effects. The virtual particle algorithm is also well suited for high-velocity impact computations, and an example is included to demonstrate this capability for a complex problem.

Keywords: Explosively formed penetrators; Contact algorithms; Explosives computations; Impact computations

1. Introduction

Three-dimensional Explosive Formed Penetrator (EFP) computations have been performed for more than 20 years [1]. These EFPs are generally formed to travel for significant distances before

*Corresponding author. Tel.: +1 612 337 3553; fax: +1 612 337 3400.
E-mail address: gordon.johnson@netaspx.com (G.R. Johnson).

0734-743X/$ - see front matter © 2005 Elsevier Ltd. All rights reserved.
doi:10.1016/j.ijimpeng.2005.01.011

delivering their kinetic energy to the intended target. The primary applications are for mining and for the defeat of armor. During the past 10 years, there has been much effort directed at forming stabilizing fins on these penetrators such that they can "fly" in a stable mode for greater distances. These finned designs require a capability to perform 3D computations. In 1993, Weimann [2] presented five different ways to form a star shaped tail and successfully demonstrated these techniques experimentally. In 1995, Bouet et al. [3] demonstrated a finned design using three detonation points. Here the results were presented for both experiments and computations. More recently there have been several efforts [4–7] that have presented both experimental results and computational results. Although there have been computed results that show good agreement with experimental results [3–7], generally the computational issues have not been addressed in these articles. This paper provides a discussion of some of the technical issues and presents some related results. It also demonstrates how a sliding/contact algorithm that works well for EFPs, is also well suited for high-velocity impact computations.

2. Technical discussion

There are three broad categories of interest that are of importance for 3D EFP (Lagrangian) computations: sliding/contact interfaces, type and arrangement of elements, and generation of the grid. The focus is on 3D axisymmetric computations with a single detonation point and no stabilizing fins.

The typical EFP considered in this article is shown in Fig. 1, along with a 2D grid and computation. The four components are a cylindrical steel case, a circular steel base plate, an iron liner with a radius of curvature, and an explosive fill. The detonation point is on the axis of symmetry, at the interface of the base plate and the explosive.

2.1. Sliding/contact algorithm

EFP computations require a very robust contact/sliding algorithm, which includes an accurate and efficient search routine. The difficulties associated with EFP computations are due to the high pressures, high detonation velocities in the explosives (that are greater than the sound velocities in the solids), and the intersection of more than two materials at a specific point. An algorithm that works well for impact problems involving mild distortions may often fail when subjected to an EFP application. It should also be noted that the discussion in this paper relates to the authors' experiences with their sliding/contact algorithms [1,8–10], as they are clearly understood by the authors. It is not appropriate to comment on undocumented strengths and weaknesses of other algorithms, as there are some very subtle details (often known only to the developers) that can make or break a sliding/contact algorithm.

The upper left portion of Fig. 2 shows a cross-section of three distinct bodies (case, liner, and explosive) that are in contact before the nodal update (at $time = t$) and that are moving in directions to cause overlap after the nodal update at the end of the integration cycle (at $time = t + \Delta t$), as shown in the upper right. As a point of reference, this is the same area as shown in the upper right portion of the EFP in Fig. 1. The three bodies are composed of elements (not shown for clarity) whose exterior faces form the sliding/contact interface, both on the

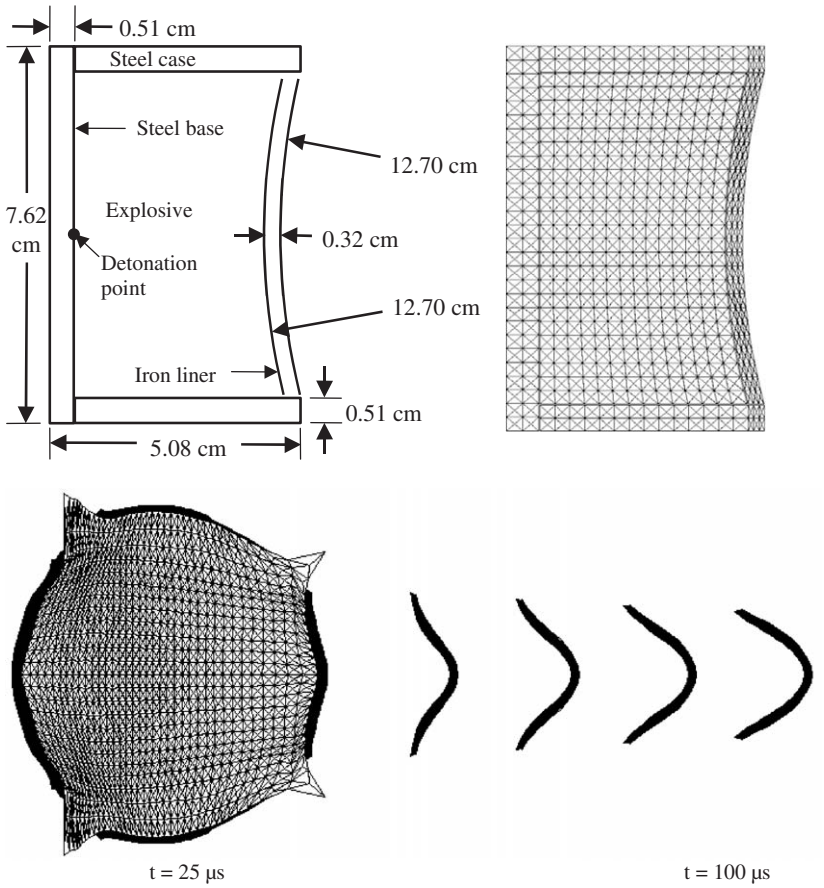

Fig. 1. Description of the EFP and a 2D computation.

cross-section shown in Fig. 2, and the third dimension normal to the cross-section. For the sliding/contact algorithm developed by the authors [8] each (slave) node that has crossed through the interface (master surface) must be adjusted to bring it back to the surface. This is accomplished by adjusting the velocities and positions of the slave and master nodes to conserve linear and angular momenta, and to provide a normal velocity match of the slave node on the master surface. The approach is symmetric (all surfaces are both slave nodes and master surfaces) and the velocity match is accomplished with an iterative technique. Furthermore, it allows for a fully automatic approach, where the user is not required to specify specific surfaces as slave and/or master.

This approach works very well provided the slave node is matched with the proper element face on the master surface. As can be seen in the upper right of Fig. 2, however, there is a very complex interaction where the three bodies meet. If the slave node is matched with the wrong portion of the master surface, the velocities and positions are incorrectly adjusted and the computation will often stop. In an effort to reduce the searching errors, the problem can be broken down into a group of slave and master surfaces. For example, in Fig. 2, there could be one interface between the case and the liner, another between the case and the explosive, and a third between the explosive and

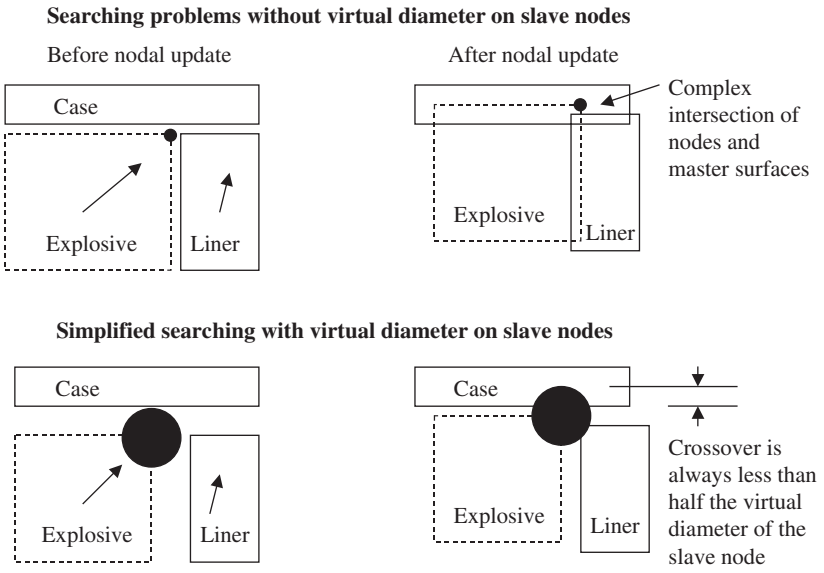

Fig. 2. Description of the searching algorithm with a virtual diameter on the slave nodes.

the liner. Although this approach has worked well in the past [1], it requires the user to specify specific interfaces and it also introduces some order-dependence into the solution.

The robustness of the searching algorithm can be significantly enhanced by considering each slave node to have a finite diameter, as shown in the lower left of Fig. 2. If this finite diameter is represented by a virtual particle, then the sliding/contact algorithm is identical to that used for meshless particles interacting with finite element grids [9,10]. A similar concept has been used by other researchers [11–13]. The diameter of the virtual particle is taken to be

$$D = 2V_{\text{ref}}\Delta t, \tag{1}$$

where V_{ref} is a reference velocity that is greater than the relative velocity of any two nodes during the course of the computation and Δt is the integration time increment. The reference velocity can generally be set to 1.1–1.5 times the initial impact velocity or detonation velocity (of the explosive). This insures that the center of the (slave) node will never cross the master surface and this allows an accurate search to be made. The virtual particle (slave node) simply interacts with the element face (master surface) with which it has the greatest crossover, as shown in the lower right of Fig. 2. Here it would be assumed to interact with the case because the crossover is greater for the case than for the liner. If a virtual particle has a significant crossover for more than one element face (master surface), then the adjustment can be made for multiple surfaces, but this is generally not necessary. Usually the match (for the next highest crossover) can be made during the next integration cycle (when it has the greatest crossover). The authors have found this approach to be very robust, but a disadvantage is that the initial grid must be generated with a small gap (equal to $D/2$) between the individual bodies. This gap is generally small enough to not affect the results of the computation, but it does provide an additional complexity when generating the grid. Note that a smaller gap is required for finer grids because the integration time increment

(Δt in Eq. (1)) is decreased as the grid becomes finer. Although it is possible to allow the virtual particle diameter in Eq. (1) to change as Δt changes, the preferred approach is to hold it constant based on a maximum (constant) Δt.

2.2. Element type and arrangement

Almost all 3D EFP (Lagrangian) computations have been performed with constant stress tetrahedral elements [14] or constant stress hexahedral (brick) elements with hourglass control [15,16]. A mixed algorithm for tetrahedral elements [17] is also considered in this paper. Fig. 3 shows tetrahedral elements arranged in a symmetric brick arrangement (24 tetrahedral elements in a brick) and a non-symmetric arrangement (6 tetrahedral elements in a brick). The symmetric arrangement has a node in the center to which all the elements are attached, and the non-symmetric arrangement has a diagonal that goes from the lower right of the front face to the upper left of the rear face. The symmetric arrangement reduces the volumetric locking sometimes associated with tetrahedral elements, whereas the non-symmetric arrangement exhibits significant locking [17]. The non-symmetric arrangement can also be used with mixed algorithms that have demonstrated a significant reduction in locking for cylinder impact computations [17]. It will later be shown that some inaccuracies are introduced by the secondary nodes (center nodes on the faces of the symmetric brick arrangement) when used for the EFP application. Finally, the hexahedral elements have no problems with locking inaccuracies, but they generally are not as robust as tetrahedral elements when subjected to severe distortions (because they can allow the grid to tangle). Tetrahedral elements, on the other hand, cannot allow the grid to tangle without going through a zero-volume configuration. Fig. 3 also shows the relative size of the individual hexahedral (brick) element, a non-symmetric arrangement of 6 tetrahedral elements (non-symmetric tets) and a symmetric arrangement of 24 tetrahedral elements (symmetric tets). For each of these conditions the volumes of the individual elements are identical ($V = h^3$). Each of the elements and arrangements considered has some advantages and some disadvantages.

2.3. Grid generation

For a circular liner in an axisymmetric EFP there are some issues regarding the generation of the grid. Fig. 4 shows the gridding approaches considered in this study. The left side gives a simple

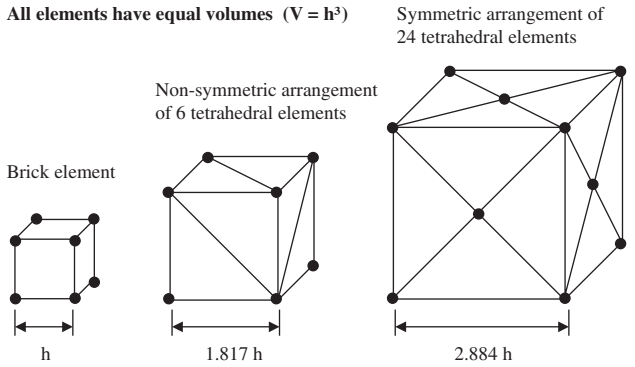

Fig. 3. Element arrangements and sizes.

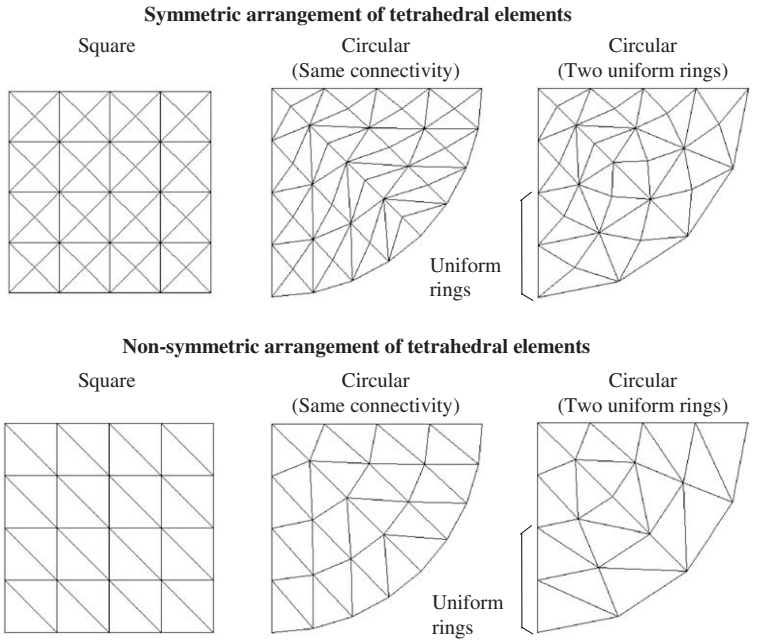

Fig. 4. Element arrangements for circular shapes.

square represented by symmetric tetrahedral elements (top) and non-symmetric tetrahedral elements (bottom). The center column shows the resulting grid for a quarter circle, using the same arrangement (connectivity) as used for the square. This approach provides elements that are approximately equally sized, but some asymmetries are introduced and some elements are not formed in a compact manner (especially along the diagonal).

In an effort to introduce more symmetry into the grid, it is possible to put uniform rings around the outer portions of the circle, as shown on the right side of Fig. 4. This provides the same number of elements in each of the uniform rings. Here the asymmetries are reduced, but the elements get larger and larger as they move outward (for a constant radial increment). Again, there are some advantages and disadvantages for both approaches.

3. Results for EFP computations

A series of computations has been performed to illustrate the effects of the issues discussed previously. A summary of these computations is provided in Table 1. The column designated by NUR/NTR is the Number of Uniform Rings (NUR) of elements (on the outer portion of the radius) and the Number of Total Rings (NTR). All of the computations used the virtual particle algorithm for sliding/contact (except for the 2D computations made for comparison). All of the 3D computations made use of a plane of symmetry such that only half of the problem was considered. An attempt was made to use approximately the same number of elements when comparing the different arrangements of symmetric and non-symmetric tetrahedral elements. The number of elements indicated in Table 1 are for the half of the problem that was included in the

Table 1
Summary of the computed results

Case	Elements	NUR/NTR	Velocity (m/s)	Length (cm)	Diameter (cm)
1	2D triangles	—	2387	3.03	5.10
2	Symmetric tets	0/12	2388	2.96	5.18
3		3/12	2384	3.01	5.00
4		6/12	2379	2.92	5.22
5		8/16	2373	2.97	5.10
6	Non-symmetric tets without mixed algorithm	0/20	2396	2.56	5.24
7		5/20	2386	2.50	5.49
8		10/20	2379	3.06	5.22
9	Non-symmetric tets with mixed algorithm	0/20	2380	3.04	4.66
10		5/20	2380	2.98	4.76
11		10/20	2372	3.08	4.85

grid. The grids are not fine enough to allow the results to fully converge, but they are fine enough to show the effects of interest, and they are coarse enough to allow the grids to be seen. The geometry of the axisymmetric EFP is shown in Fig. 1. The liner is Armco iron, the case and the base plate are 4340 steel and the explosive is Octol. The Johnson–Cook model is used for the metals [18] and the Gamma law (with programmed burn) is used for the explosive [1].

For the liner in the 3D symmetric tetrahedral element grid there are 144 triangular faces on the plane of symmetry (for the radius). This is the result of 12 rings of symmetric bricks times 3 layers through the thickness times 4 triangular faces per symmetric brick. For the 3D liner there are 20,736 tetrahedral elements in the grid (for no uniform rings). An axisymmetric 2D computation was performed to provide comparisons to the 3D computations. It is not an obvious procedure to select a 2D grid that is comparable to a 3D grid. The 2D grid is shown in the upper right of Fig. 1 and it is identical to the 3D symmetric tet grid on the plane of symmetry. The computed response for the 2D simulation is shown on the bottom of Fig. 1. Failure of the metals was not allowed and the explosive gases were dropped from the computation at $t = 25\,\mu s$.

Fig. 5 shows the grids for four of the cases. The grid in the upper left uses the symmetric arrangement of tetrahedral elements without any uniform ring (NUR/NTR $= \frac{0}{12}$), and the grid in the upper right uses the symmetric arrangement with six uniform rings on the outer half of the radius (NUR/NTR $= \frac{6}{12}$). The grid in the lower left uses the non-symmetric arrangement of tetrahedral elements without any uniform rings (NUR/NTR $= \frac{0}{20}$), and the grid in the lower right uses the non-symmetric arrangement with 10 uniform rings on the outer half of the radius (NUR/NTR $= \frac{10}{20}$). Not shown in Fig. 5 are two additional grids which have uniform rings for the outer $\frac{1}{4}$ of the radius (NUR/NTR $= \frac{3}{12}$ for the symmetric arrangement and NUR/NTR $= \frac{5}{20}$ for the non-symmetric arrangement).

The computed results of nine computations are shown in Figs. 6 and 7. The top three computations are for a symmetric grid, the center row is for a non-symmetric grid, and the bottom row is for a non-symmetric grid that uses a mixed algorithm [17]. It is evident from Fig. 7 that the non-symmetric grid produces non-circular liner formations, with and without uniform rings, and

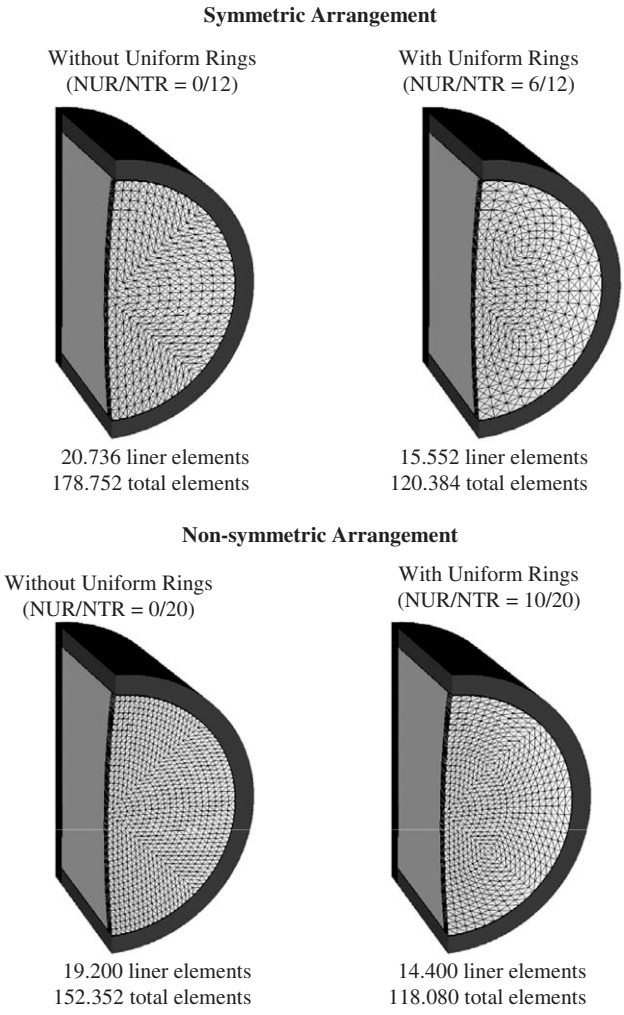

Fig. 5. Initial grids for symmetric and non-symmetric arrangements, with and without uniform rings.

with and without the mixed algorithm. It appears that the mixed algorithm exhibits less locking inasmuch as the $\mathrm{NUR/NTR} = \frac{0}{20}$ case (lower left in Fig. 7) has more buckling than the comparable case without the mixed algorithm. For this application the mixed algorithm does not provide significantly improved results as it did previously for cylinder impact computations [17], but this is probably due to the errors introduced by the non-symmetric grid arrangement, and the associated non-symmetric nodal mass distribution. For low-pressure, plastic-flow computations (such as the cylinder impact computations) the asymmetries (grid and nodal mass distribution) do not have a significant effect. For explosive shock wave computations it does make a difference, however, as shown (in Fig. 6) by the distinct deformation patterns at angular intervals of $\pi/4$ rad on the surface of the liner (where the diagonal orientations of the non-symmetric grid are changed). In all cases, however, the automatic sliding/contact algorithm, with the virtual particles described previously, performed in an accurate and robust manner.

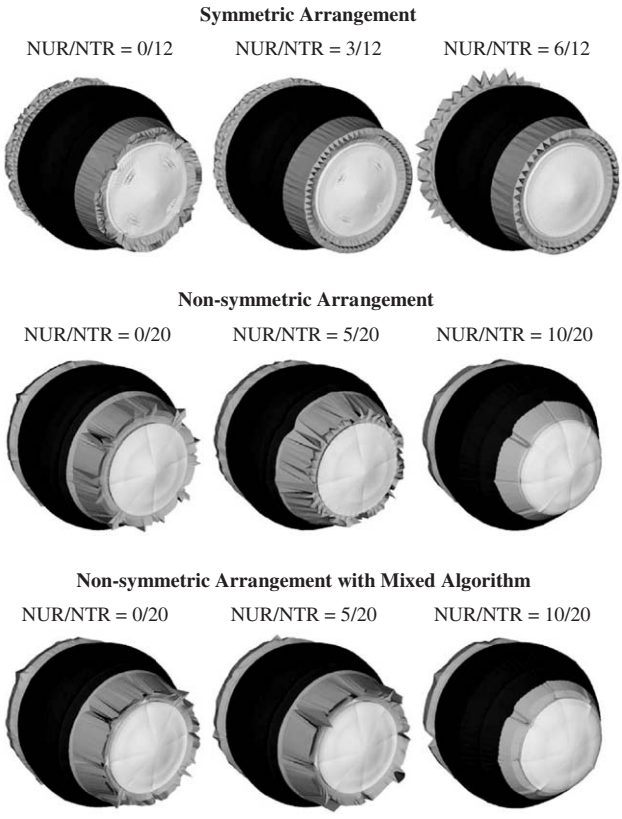

Fig. 6. Computed responses at 25 μs after detonation.

The results for the symmetric arrangement of elements also produce some interesting characteristics. For no uniform rings (NUR/NTR $= \frac{0}{12}$) and for three uniform rings on the outer $\frac{1}{4}$ of the radius (NUR/NTR $= \frac{3}{12}$) the outer portion of the liner tends to form into a buckling pattern. This is due to the asymmetries along the diagonals of the initial grid. For these same two cases the elements on the outer diagonals of the non-uniform rings tend to form a rough surface, with the secondary (center) nodes of the symmetric brick arrangement poking outward. These secondary nodes have fewer elements attached to them and they have a corresponding lower mass. The affected elements on the diagonal are also not as compact as the elements on the uniform rings. While this phenomena would probably not occur under static loading, the specific shock loading from the explosive produces this strange deformation pattern.

The computed result in the upper right is symmetric and does not have any of the rough surface effects. It uses a symmetric grid and uniform rings on the outer half of the radius (NUR/NTR $= \frac{6}{12}$). It could be argued that the buckling pattern in the other two symmetric computations is correct, and that the courser grid of the uniform rings does not allow the buckling to occur. To test this possibility, another computation was performed with a finer grid (16 symmetric rings instead of 12) and it did not buckle. Therefore, it would appear from the computations presented herein that the best results are achieved with a symmetric arrangement of

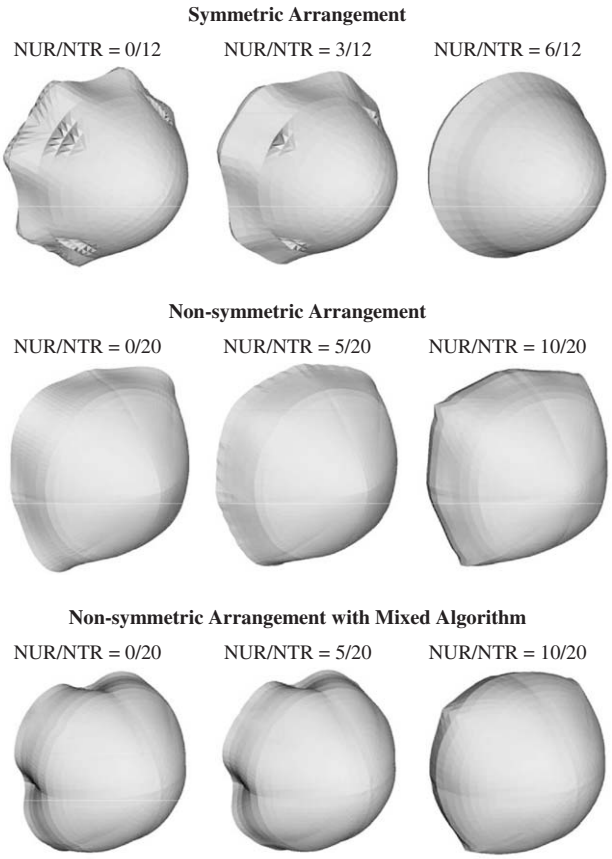

Fig. 7. Final liner shapes at 100 μs after detonation.

elements and with uniform rings on the outer half of the radius. A similar conclusion was reached by Maudlin [19] in another study.

A further comparison of the results is shown in the cross-sections of the liners in Fig. 8. Here the darkened elements represent elements with equivalent plastic strains greater than 0.7. As expected, there are some distinct differences. Fig. 9, however, shows some strong similarities in the cross-sections. The 2D axisymmetric computation (from Fig. 1) is shown on the left and the 3D computation (from the upper right of Figs. 6–8) is shown in the center of Fig. 9. The 3D computation on the right is from the aforementioned finer grid (with symmetric elements and uniform rings on the outer half of the radius). In addition to similar strain distributions, the velocities and geometric shapes are even more similar (as shown in Table 1).

4. Example of high-velocity impact computation

A closely related problem that requires a robust sliding/contact algorithm is that of high-velocity impact for complex geometries. Such an example is shown in Fig. 10. It consists of a

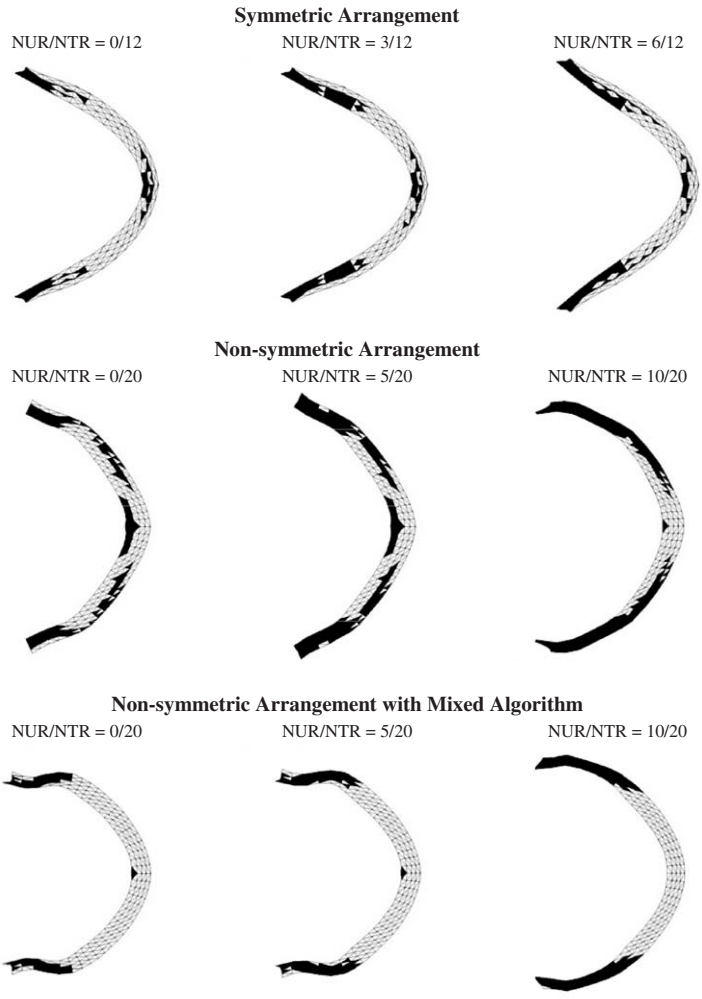

Fig. 8. Equivalent plastic strains (ε_p) on cross-sections at 100 μs after detonation (darkened elements have $\varepsilon_p > 0.7$).

projectile, with a tungsten core and a copper sleeve, impacting a three-layer target (7039 aluminum, 1006 steel, 4340 steel) at a velocity of $V = 2032\,\mathrm{m/s}$ and an obliquity of 30°. All five of the materials interact with one another through contact and sliding. For this problem, the tetrahedral elements are automatically converted into meshless particles when they become highly strained [10]. The Generalized Particle Algorithm (GPA) is used for the meshless particles [9,10], the materials are represented with the Johnson–Cook strength and failure models [18,20], and the sliding/contact algorithm uses the virtual particle algorithm described herein. It can be seen that the distortions are severe, that there is significant contact and sliding between the different materials, and that the failed material behind the target is represented. For this class of problems the virtual particle algorithm (shown in the lower portion of Fig. 2) is much more robust than a comparable algorithm that does not use virtual particles (shown in the upper portion of Fig. 2).

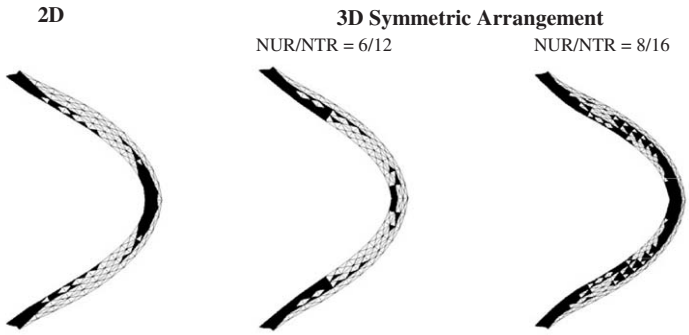

Fig. 9. Comparison of equivalent plastic strains (ε_p) for 2D axisymmetric computation and 3D computations with a symmetric arrangement and uniform rings on the outer half of the radius (darkened elements have $\varepsilon_p > 0.7$).

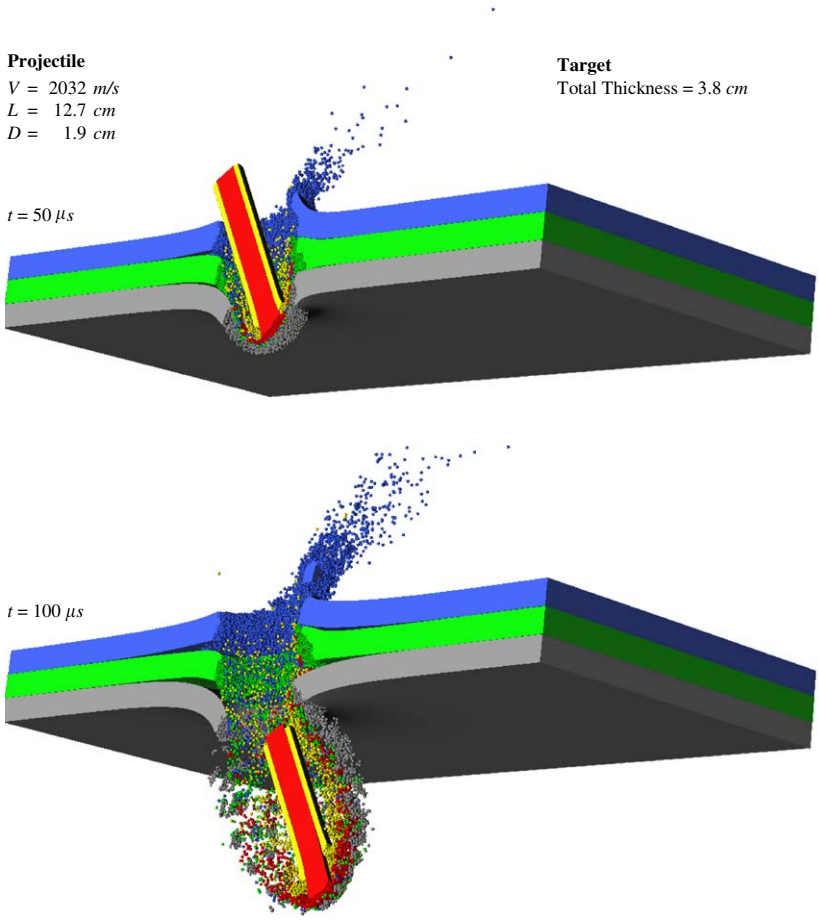

Fig. 10. Complex computation of a tungsten/copper projectile impacting a three-layer target (7039 aluminum/1006 steel/4340 steel) at an impact velocity of 2032 m/s.

Again, the reason that the virtual particle algorithm is more robust is that every slave node (with a virtual particle diameter) can always find the proper master surface with which it should interact.

5. Summary and conclusions

This paper has focused on some considerations for 3D EFP computations. A virtual particle approach for sliding/contact has been presented, and parametric computations have been performed for various element and grid arrangements. The symmetric arrangement of tetrahedral elements, with uniform rings along the outer half of the radius, provided the best results. Significant differences occurred with other element and grid arrangements. The virtual particle algorithm is very robust, both for the 3D EFP computations and for an example impact computation with high distortions and several materials.

Acknowledgments

The research reported in this article was performed in connection with contract DAAD19-03-D-0001 with the US Army Research Laboratory and contract F08630-02-M-0077 with the US Air Force Research Laboratory. The views and conclusions contained in this article are those of the authors and should not be interpreted as presenting the official policies or positions, either expressed or implied, of the US Army Research Laboratory, the US Air Force Research Laboratory, or the US Government unless so designated by other authorized documents. Citation of manufacturer's or trade names does not constitute an official endorsement or approval of the use thereof. The US government is authorized to reproduce and distribute reprints for Government purposes notwithstanding any copyright notation hereon.

References

[1] Johnson GR. Dynamic analysis of explosive-metal interaction in three dimensions. J Appl Mech 1981;103:30–4.
[2] Weimann K. Flight stability of EFP with star shaped tail. Proceedings of the 14th international symposium on ballistics, Quebec City, Canada; September 1993. p. 755–63.
[3] Bouet T, Tarayre P, Guillon JP. Study of a multi-point ignition EFP. Proceedings of the 15th international symposium on ballistics, Jerusalem, Israel; May 1995. p. 159–66.
[4] Carleone J, Bender D. A unique method of providing an explosively formed penetrator with fins. Proceedings of 17th international symposium on ballistics, Midrand, South Africa; March 1998. p. 55–62.
[5] Ng W, Fong R, Rice B. Hydrocode 3D simulation of non-axisymmetric explosively formed penetrator (EFP) warheads. Proceedings of 17th international symposium on ballistics, Midrand, South Africa; March 1998. p. 481–7.
[6] Bender D, Chhouk B, Fong R, Ng W, Rice B, Volkmann E. Explosively formed penetrators (EFP) with canted fins. Proceedings of 19th international symposium on ballistics, Interlaken Switzerland; May 2001. p. 755–62.
[7] Ng W, Fong R, Weimann K. Nonaxisymmetric waveshaped EFP warheads. Proceedings of 20th international symposium on ballistics, Orlando, Florida. p. 582–8.
[8] Johnson GR, Stryk RA. Symmetric contact and sliding interface algorithms for intense impulsive loading. Comput Methods Appl Mech Eng 2001;190:4531–49.

[9] Johnson GR, Beissel SR, Stryk RA. An improved generalized particle algorithm that includes boundaries and interfaces. Int J Numer Meth Eng 2002;53:875–904.
[10] Johnson GR, Stryk RA. Conversion of 3D distorted elements into meshless particles during dynamic deformation. Int J Impact Eng 2003;28:947–66.
[11] Belytschko T, Neal MO. Contact-impact by the pinball algorithm with penalty and Lagrangian methods. Int J Numer Meth Eng 1991;31:547–72.
[12] Whirley RG, Englemann BE. Automatic contact algorithm in DYNA3D for crashworthiness and impact problems. Nucl Eng Des 1994;150:225–33.
[13] Thoma K, Vinckier D. Numerical simulation of a high velocity impact on fiber reinforced materials. Nucl Eng Des 1994;150:441–52.
[14] Johnson GR, Colby DD, Vavrick DJ. Three-dimensional computer code for dynamic response of solids to intense impulsive loads. Int J Numer Meth Eng 1979;14:1865–71.
[15] Flanagan DP, Belytschko T. A uniform strain hexahedron and quadrilateral with orthogonal hourglass control. Int J Numer Meth Eng 1981;17:679–706.
[16] Belytschko T, Ong JSJ, Liu WK, Kennedy JM. Hourglass control in linear and nonlinear problems. Comput Methods Appl Mech Eng 1984;43:251–76.
[17] Beissel SR, Johnson GR. Large-deformation triangular and tetrahedral element formulations for unstructured meshes. Comput Methods Appl Mech Eng 2000;187:469–82.
[18] Johnson GR, Cook WH. A constitutive model and data for metals subjected to large strains, high strain rates and high temperatures. Proceedings of seventh international symposium on ballistics, The Hague, The Netherlands; April 1983. p. 541–7.
[19] Maudlin PJ. Personal communication; 2004.
[20] Johnson GR, Cook WH. Fracture characteristics of three metals subjected to various strains, strain rates, temperatures and pressures. Eng Fract Mech 1985;21:31–48.